

SnO_x Atomic Layer Deposition on Bare Perovskite—An Investigation of Initial Growth Dynamics, Interface Chemistry, and Solar Cell Performance

Adam Hultqvist,* T. Jesper Jacobsson, Sebastian Svanström, Marika Edoff, Ute B. Cappel, Håkan Rensmo, Erik M. J. Johansson, Gerrit Boschloo, and Tobias Törndahl



Cite This: *ACS Appl. Energy Mater.* 2021, 4, 510–522



Read Online

ACCESS |

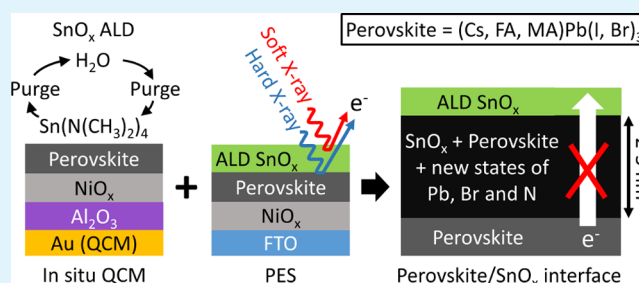
Metrics & More

Article Recommendations

Supporting Information

ABSTRACT: High-end organic–inorganic lead halide perovskite semitransparent p–i–n solar cells for tandem applications use a phenyl-C₆₁-butyric acid methyl ester (PCBM)/atomic layer deposition (ALD)-SnO_x electron transport layer stack. Omitting the PCBM would be preferred for manufacturing, but has in previous studies on (FA,MA)Pb(Br,I)₃ and (Cs,FA)Pb(Br,I)₃ and in this study on Cs_{0.05}FA_{0.79}MA_{0.16}PbBr_{0.51}I_{2.49} (perovskite) led to poor solar cell performance because of a bias-dependent light-generated current. A direct ALD-SnO_x exposure was therefore suggested to form a nonideal perovskite/SnO_x interface that acts as a transport barrier for the light-generated current. To further investigate the interface formation during the initial ALD SnO_x growth on the perovskite, the mass dynamics of monitor crystals coated by partial p–i–n solar cell stacks were recorded in situ prior to and during the ALD using a quartz crystal microbalance. Two major finds were made. A mass loss was observed prior to ALD for growth temperatures above 60 °C, suggesting the decomposition of the perovskite. In addition, a mostly irreversible mass gain was observed during the first exposure to the Sn precursor tetrakis(dimethylamino)tin(IV) that is independent of growth temperature and that disrupts the mass gain of the following 20–50 ALD cycles. The chemical environments of the buried interface were analyzed by soft and hard X-ray photoelectron spectroscopy for a sample with 50 ALD cycles of SnO_x on the perovskite. Although measurements on the perovskite bulk below and the SnO_x film above did not show chemical changes, additional chemical states for Pb, Br, and N as well as a decrease in the amount of I were observed in the interfacial region. From the analysis, these states and not the heating of the perovskite were concluded to be the cause of the barrier. This strongly suggests that the detrimental effects can be avoided by controlling the interfacial design.

KEYWORDS: perovskite solar cell, ALD, in situ QCM, HAXPES, interface, SnO_x



1. INTRODUCTION

The solar cell is one of the main technologies to generate renewable energy. One family of solar cell materials that has been of special interest lately is hybrid organic–inorganic lead halide perovskites, hereafter denoted as perovskites. This is not only because of the excellent properties of the material such as high light absorption and long free charge carrier diffusion length¹ but also because of how straightforward it is to synthesize the material with high quality.² Solar cells using these perovskite materials as absorbers have already reached efficiency beyond 25%³ but are often found to have stability issues under long-term operation. The focus of the research field has therefore expanded to include understanding and solving the above-said stability issues, while still maintaining good solar cell performance.⁴

The stability of the perovskite solar cells is not only dependent on the perovskite itself but also to a large degree on the charge carrier transport materials that form direct

interfaces to the perovskite film.^{4,5} Inorganic materials would be the preferred choice for these transporting layers as they typically have a higher resilience to heat, light, mechanical stress, and the local chemical environment. From an upscaling standpoint, they are also costly.⁶ However, the interfaces formed between the perovskite and inorganic materials have, with the exception of TiO₂, not been found to be as good for carrier transport and electrical surface passivation as that when the interfaces are formed between the perovskite and organic materials.⁷ This problem is in general more severe when the inorganic layer is deposited directly onto the perovskite as

Received: September 29, 2020

Accepted: December 18, 2020

Published: January 4, 2021



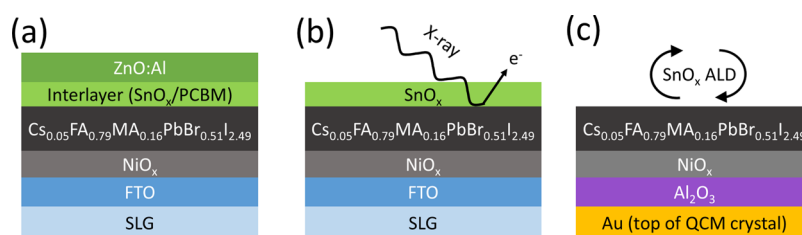


Figure 1. Different sample stacks for (a) p-i-n solar cell evaluation, (b) PES analysis of the buried SnO_x/perovskite interface, and (c) QCM monitoring of mass changes during the SnO_x ALD exposure of bare perovskite.

compared to that when the perovskite is deposited onto the inorganic layer.⁴

Depositing inorganic films directly on the perovskite is not straightforward as the deposition process has to account for the stability of the perovskite in terms of heat, chemical exposure, and material softness. So far, the most successful deposition processes have been using spin coating of inorganic particles with minor postannealing and very slow evaporation without substrate heating, where the thermal energy is kept low and no aggressive chemicals are introduced.^{8,9} Unfortunately, the resulting interfaces and films have not been able to perform as well as their organic counterparts or as well as that when the perovskite is deposited onto the inorganic layers.^{8–10}

Thermally activated atomic layer deposition (ALD) should be a good candidate to grow high-quality inorganic films directly onto the perovskite, as it uses a relatively low deposition temperature and does not rely on adding energy to the surface from incoming species. It does however rely on chemical reactions. So far, most studies that perform ALD directly on perovskites have shown that the employed chemistry is too reactive and damages the perovskite surface or even bulk.^{11–22} The amount of available ALD chemistries and growth conditions is however large,^{23–25} and there are thus a lot of possibilities to alter the growth process in order to form a more intact perovskite/inorganic interface. Studies have also shown that even if the surface does become modified, thin layers of Al₂O₃ can still be grown by ALD directly on the perovskite and improve both solar cell performance and long-term stability.^{26,27} A parallel study also showed that TiO₂ could successfully be deposited on (Cs,FA)Pb(Br,I)₃.²²

Similarly, previous studies and a parallel study have shown that high-quality SnO_x can be grown on (FA,MA)Pb(Br,I)₃ and (Cs,FA)Pb(Br,I)₃ surfaces as an electron transport layer (ETL) using a thermal ALD process with tetrakis-(dimethylamino)tin(IV) (TDMASn) and H₂O as the precursors, without harming the perovskite bulk.^{17,18,22} The resulting solar cell performance was unfortunately found to be low, despite the seemingly successful process, and upon closer inspection, an interface layer was identified as a possible cause of failure.^{17,18,22}

In contrast, SnO_x was found to be one of the best performing inorganic ETLs for the regular stack (n-i-p) solar cell in a previous study,²⁸ which indicates that the SnO_x/perovskite interface can be made benign and that the band alignment for electron transport out of the perovskite is good. SnO_x also has other benefits such as less photocatalytic activity compared to TiO₂, higher transparency to sunlight, high chemical stability, and high thermal stability. Thus, to be able to include SnO_x as the ETL in the inverted stack (p-i-n) is very interesting to increase the performance and stability. Because SnO_x is transparent and able to withstand subsequent

processing such as sputtering of, for example, transparent conducting oxides (TCO), it also makes an ideal candidate for an ETL in a perovskite top cell for tandem applications. In fact, all of the high-end tandem solar cells using perovskite top cells already utilize SnO_x as part of their ETL stack.^{29–32} In these cases the perovskite is protected using a thin layer of either C₆₀ or phenyl-C₆₁-butyric acid methyl ester (PCBM) prior to the SnO_x ALD deposition. As mentioned above, moving away from using organic layers would be preferable for several reasons. To achieve this, it is imperative to continue working on forming high-quality junctions between perovskites and inorganic materials such as SnO_x. A key to success would be to identify how the detrimental interface is formed when the perovskite is exposed to the SnO_x ALD process and whether it can be prevented.

In this study, the Cs_{0.05}FA_{0.79}MA_{0.16}PbBr_{0.51}I_{2.49}/ALD SnO_x interface is therefore investigated in more detail by studying the in situ mass change dynamics of the initial SnO_x film growth at different temperatures and conditions using perovskite-coated quartz crystal resonators as substrates. Soft and hard X-ray photoelectron spectroscopy (SOXPES and HAXPES) analyses are also used to analyze the chemistry of the buried perovskite/SnO_x interface beneath a thin SnO_x film. Finally, to separate the influence of the SnO_x bulk properties from the interfaces created by the ALD precursor exposure, n-i-p solar cells where SnO_x is grown before the perovskite and p-i-n solar cells where SnO_x is grown either directly onto the perovskite or onto a perovskite that is protected with a thin PCBM film are synthesized and evaluated.

2. RESULTS

2.1. Test Structures. To investigate the interface, we design our test structures around semitransparent perovskite p-i-n solar cells as they are currently one of the prime examples where a direct ALD of SnO_x on perovskite could be beneficial. The full semitransparent p-i-n solar cell stack (see Figure S15 in the Supporting Information for optical details) in this study was fluorine-doped tin oxide (FTO)/NiO_x/Cs_{0.05}FA_{0.79}MA_{0.16}PbBr_{0.51}I_{2.49}/interlayer/ZnO/Al, as shown in Figure 1a, and it was used to evaluate the resulting solar cell performance from changing the interlayer. In addition to an interlayer of only SnO_x, two variants using either only PCBM or PCBM/SnO_x are introduced as references. PCBM has previously shown excellent ETL performance for perovskites^{9,10} but has not been able to withstand the subsequent sputtering of TCO that typically follows in the semitransparent p-i-n solar cell stack.^{29–32} It has however shown success in protecting the perovskite from the SnO_x ALD process, and as SnO_x was able to protect the perovskite and PCBM from the TCO sputtering, a stack of PCBM/SnO_x or C₆₀/SnO_x that behaves similarly has therefore been included in most

semitransparent p–i–n solar cells.^{29–32} In order to analyze the perovskite/SnO_x interface using surface-sensitive photoelectron spectroscopy (PES), the TCO top layer was omitted and the thickness of SnO_x was varied. The resulting test structure, shown in Figure 1b, was FTO/NiO_x/Cs_{0.05}FA_{0.79}MA_{0.16}PbBr_{0.51}I_{2.49}, where the perovskite surface was either left uncoated or was coated by SnO_x using 50 or 500 ALD cycles. To perform QCM monitoring of the mass changes during the SnO_x ALD exposure of bare perovskite, the p–i–n solar cell stack was further adapted. On delivery, the monitor crystals came with a Au coating, but Au has been shown to diffuse into perovskites and organic layers.³³ The monitor crystals were therefore coated with an Al₂O₃ diffusion barrier for precaution using a low-temperature ALD process. As the monitor crystals cannot withstand the high temperatures required for the postannealing of FTO, the layer was omitted in the stack and NiO_x was therefore deposited directly on Al₂O₃. Figure 1c shows the resulting Au/Al₂O₃/NiO_x/Cs_{0.05}FA_{0.79}MA_{0.16}PbBr_{0.51}I_{2.49} sample stack used for the QCM measurements. Further details regarding the sample synthesis and sample analysis using current density–voltage (*J*–*V*), PES, and QCM are found in the Experimental Methods section below.

2.2. Quartz Crystal Microbalance Measurements.

2.2.1. Heating of Perovskite Films. To stabilize the substrate temperature, the in-house baseline ALD process used a 1800 s preheating step in a 4 Torr N₂ environment prior to deposition.³⁴ As a perovskite is known to decompose at elevated temperatures, the mass change over time for the Cs_{0.05}FA_{0.79}MA_{0.16}PbBr_{0.51}I_{2.49} perovskite-coated quartz crystals in the 4 Torr N₂ environment was monitored at 60, 90, and 120 °C, and the mass changes are shown in Figure 2. Although

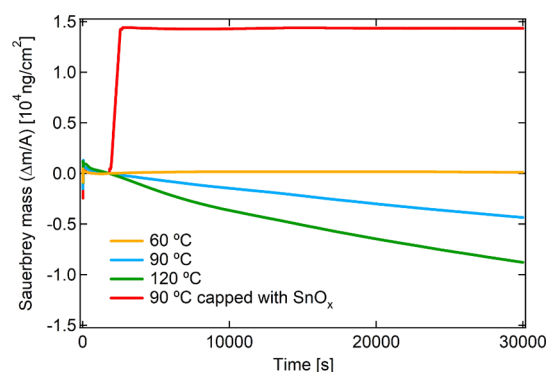


Figure 2. Mass changes of Cs_{0.05}FA_{0.79}MA_{0.16}PbBr_{0.51}I_{2.49} perovskite-coated QCM crystals because of extended heating in the ALD reactor at different temperatures. A sample where the perovskite is first heated uncoated for 1800 s and then coated by SnO_x using a short CVD stage followed by 275 ALD cycles is also shown for comparison. The curves have been shifted to 0 ng/cm² at 1800 s.

the mass remains stable over time at a temperature of 60 °C, a continuous mass loss is observed at both 90 and 120 °C. The calculated mass loss rate is approximately 0.13 ng/cm² s at 90 °C and 0.22 ng/cm² s at 120 °C, which for every second corresponds to 0.2 and 0.3%, respectively, of the mass gained per SnO_x ALD cycle at 90 °C. Furthermore, the mass loss per second is larger at 120 °C as compared to that at 90 °C. In contrast, Figure 2 also shows a sample at 90 °C that has, after an 1800 s heat-up time prior to deposition, been coated with SnO_x by a short chemical vapor deposition (CVD) stage and

then exposed to 275 ALD cycles. In this case, it is clear that the mass loss over time ceases after SnO_x capping. Thus, the process that leads to the mass loss during heating is induced by having an uncoated perovskite surface but can be prevented by capping the surface with SnO_x.

2.2.2. Influence of Precursor Exposure. Normal ALD process conditions are mimicked to test the influence of TDMASn and water precursor exposures on Cs_{0.05}FA_{0.79}MA_{0.16}PbBr_{0.51}I_{2.49} perovskite films. After heating the substrate at 90 °C for 1800 s under 4 Torr of N₂ in the ALD reactor, the perovskite is exposed to a 1 s pulse of either TDMASn or H₂O, and the resulting mass changes along with an unexposed reference sample are shown in Figure 3. No

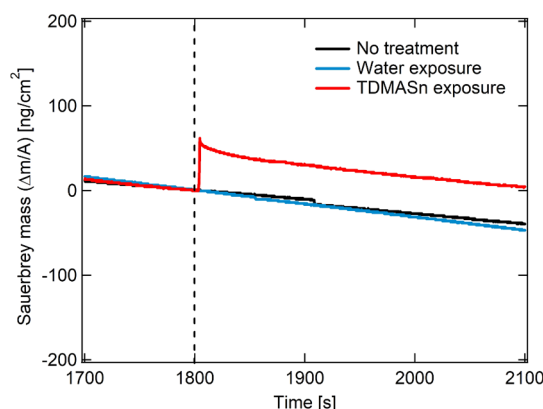


Figure 3. Mass changes of the Cs_{0.05}FA_{0.79}MA_{0.16}PbBr_{0.51}I_{2.49} perovskite-coated QCM crystal because of 1 s of DI H₂O or 1 s of TDMASn precursor exposures after 1800 s (dashed line) of heating at 90 °C. For comparison, an untreated reference is also included, and all of the curves are shifted to 0 ng/cm² at 1800 s.

change in mass besides the slow loss over time is detected for the reference sample, as expected. The same observation is also made for the sample exposed to water vapor, despite water being a known source of degradation for inorganic/organic hybrid perovskites.⁴ For the TDMASn precursor, there is a clear mass gain during the pulse that persists after exposure and that corresponds to 1.6 cycles of ALD SnO_x growth at 90 °C. Then follows a slow mass loss at a similar rate as for the uncoated perovskite. A continuous exposure of TDMASn gives a stabilized mass gain rate after a few seconds that is kept until the pulse is over, where after the slow mass loss seen for the uncoated sample resumes (Figure S3 in the Supporting Information).

2.2.3. Growth of SnO_x on Perovskite. Figure 4a shows how the mass of the Cs_{0.05}FA_{0.79}MA_{0.16}PbBr_{0.51}I_{2.49} perovskite-coated QCM crystal changes during a 500-cycle ALD SnO_x process at 90 °C. Initially, the mass gain/time or rather the mass gain/cycle of SnO_x is slow because of the chemistry of the substrate, in this case the perovskite, inhibiting the SnO_x ALD growth. The mass gain/cycle slowly increases over time as SnO_x grows more and more on itself and less on the perovskite until it finally saturates as SnO_x only grows on SnO_x. To illustrate the mass dynamics of the individual ALD cycles, Figure 4b shows five SnO_x ALD cycles (0.4 s TDMASn/0.8 s N₂ purge/0.4 s H₂O/0.8 s N₂ purge) during the saturated growth regime. The mass gain only occurs during the TDMASn pulses (highlighted red in Figure 4b). In the following N₂ purge (highlighted blue in Figure 4b), a little bit of mass is initially lost, possibly because of the desorption of

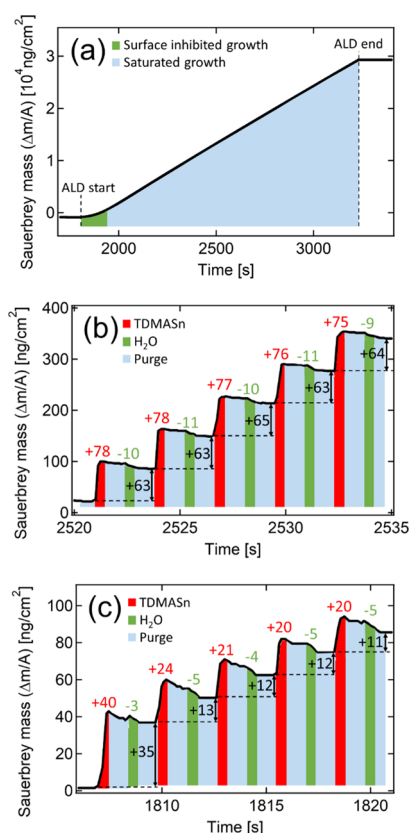


Figure 4. (a) Overall mass gain of a $\text{Cs}_{0.05}\text{FA}_{0.79}\text{MA}_{0.16}\text{PbBr}_{0.51}\text{I}_{2.49}$ perovskite-coated QCM crystal from a 500-cycle SnO_x ALD process deposited at 90 °C and started at 1800 s. Close-up images of (a) showing (b) five cycles of the saturated growth regime, and (c) first five cycles of the ALD process. TDMASn (red), H_2O (green), and purge (light blue) have been highlighted in (b,c) to show the ALD cycle. The change in mass during the TDMASn pulses (red), H_2O pulses (green), and ALD cycles (black) is also shown in (b,c). (b) and (c) use the same time axis as (a) for comparison but have been shifted in mass.

unreacted TDMASn. A more distinct mass loss follows during the water pulse (highlighted green in Figure 4b) as $-\text{DMA}$ ligands still bound to the SnO_x surface are in the ideal case exchanged for the lighter $-\text{OH}$ groups, forming $\text{H}-\text{DMA}$ as a reaction product. From the PES analysis below, it was however apparent that the SnO_x film contains both C and N, indicating that the intended ALD reaction is not always complete. During the following N_2 purge (highlighted blue in Figure 4b), the mass remains almost unchanged. Figure 4b also shows the mass gain for each individual TDMASn pulse, mass loss for every H_2O pulse, and mass gain for each ALD cycle, all of which nicely correspond to the respective averages of 77 ± 5 , -10 ± 5 , and 64 ± 5 ng/cm^2 for the saturated growth regime. In contrast, the mass changes during the first five ALD cycles shown in Figure 4c are not as large and not as consistent as that for the film-on-film growth. The most striking observation is that the mass gain for the first TDMASn pulse is 40 ng/cm^2 compared to the approximately 20 ng/cm^2 gain per pulse for the following cycles. Unlike the initial TDMASn pulse dynamics, the mass loss during the first H_2O pulse is small but slowly becomes larger for subsequent cycles. Except for the first cycle with a mass gain of 35 ng/cm^2 , the mass gain/cycle starts out small at around 10–15 ng/cm^2 . From there, it gradually increases for about 50 cycles until it reaches the

saturated value of 64 ± 5 ng/cm^2 discussed above. For comparison, when the SnO_x process nucleates on the gold surface of an uncoated QCM crystal, it requires fewer cycles (about 15) to reach a saturated growth per cycle, and the initial mass change is not as pronounced (Figure S1a in the Supporting Information). The initial growth per cycle and mass changes per pulse are also closer to those of the saturated growth regime of the same process (Figure S1b in the Supporting Information).

The initial mass dynamics of the SnO_x ALD process grown on perovskite at 60, 90, and 120 °C are shown in Figure 5a.

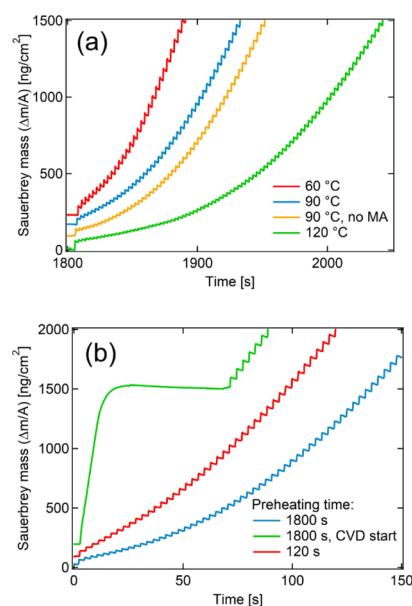


Figure 5. (a) Initial mass gain dynamics of the 500-cycle SnO_x ALD process that started at 1800 s for the $\text{Cs}_{0.05}\text{FA}_{0.79}\text{MA}_{0.16}\text{PbBr}_{0.51}\text{I}_{2.49}$ and the MA-free $\text{Cs}_{0.17}\text{FA}_{0.83}\text{PbBr}_{0.51}\text{I}_{2.49}$ perovskite-coated QCM crystals as a function of (a) temperature and perovskite composition, and (b) starting conditions of the 90 °C process. For an easier comparison, the curves have been shifted in mass in (a) and in mass and time in (b).

The 60 and 120 °C processes show the same type of mass dynamics for TDMASn exposure as for the 90 °C process discussed above. Thus, there is a large mass gain for the first TDMASn pulse of 40–60 ng/cm^2 and then smaller mass gains for the following TDMASn pulses that slowly increase for each pulse until reaching the saturated growth regime. This process takes more pulses as the temperature increases, and the implication of this is that the mass gain per cycle will follow a similar trend, as shown in Figure 5a. It is interesting to note that even the sample at 60 °C where no mass loss was observed prior to the ALD deposition still shows the same trend for the initial mass dynamics. As shown in Figure 5a, the general mass dynamics are also kept when the 90 °C ALD process is performed on MA-free $\text{Cs}_{0.17}\text{FA}_{0.83}\text{PbBr}_{0.51}\text{I}_{2.49}$ perovskite films, but the number of cycles to reach the saturated mass gain per cycle is at the same time slightly increased. We observe this in general for our experiments on MA-free $\text{Cs}_{0.17}\text{FA}_{0.83}\text{PbBr}_{0.51}\text{I}_{2.49}$ even at other temperatures and conditions not shown.

Figure 5b shows that very similar mass dynamics were also achieved when the preheating time was reduced from the baseline 1800 s to 120 s for the 90 °C process in an attempt to

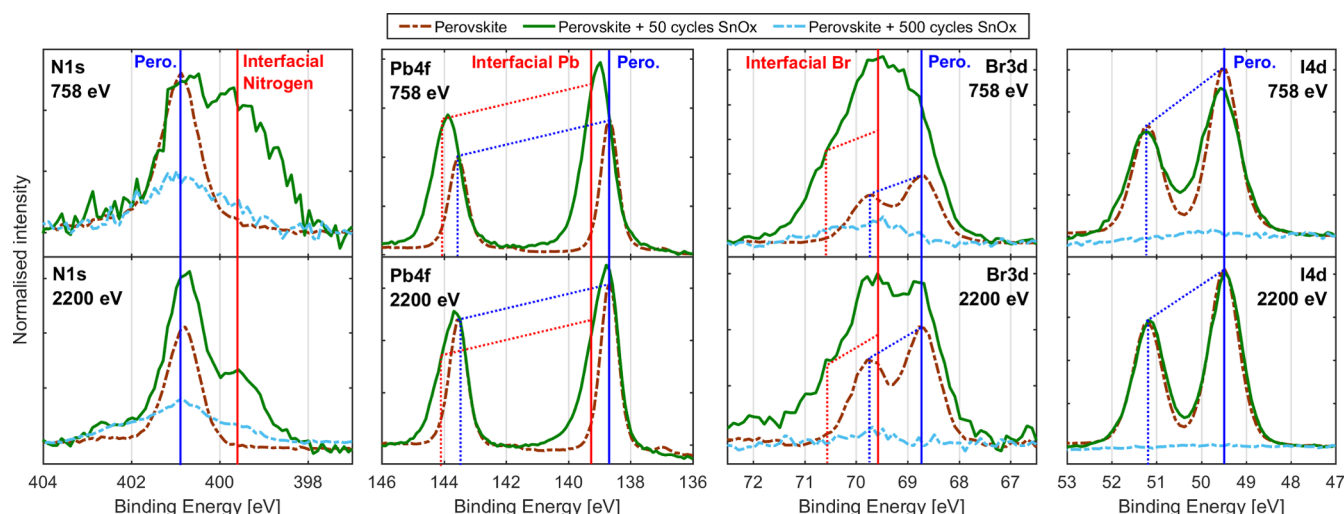


Figure 6. N 1s, Br 3d, Pb 4f, and I 4d core levels measured with photon energies of 758 and 2200 eV. Intensities are normalized to I 4d and Sn 3d total area for the perovskite and perovskite + 500 cycles of SnO_x, respectively. The binding energy is calibrated against Au 4f_{7/2} at 84 eV. Vertical lines indicate the peak positions obtained from the curve-fitting analysis of 2200 eV, with the spin–orbit doublet positions indicated by dashed lines.

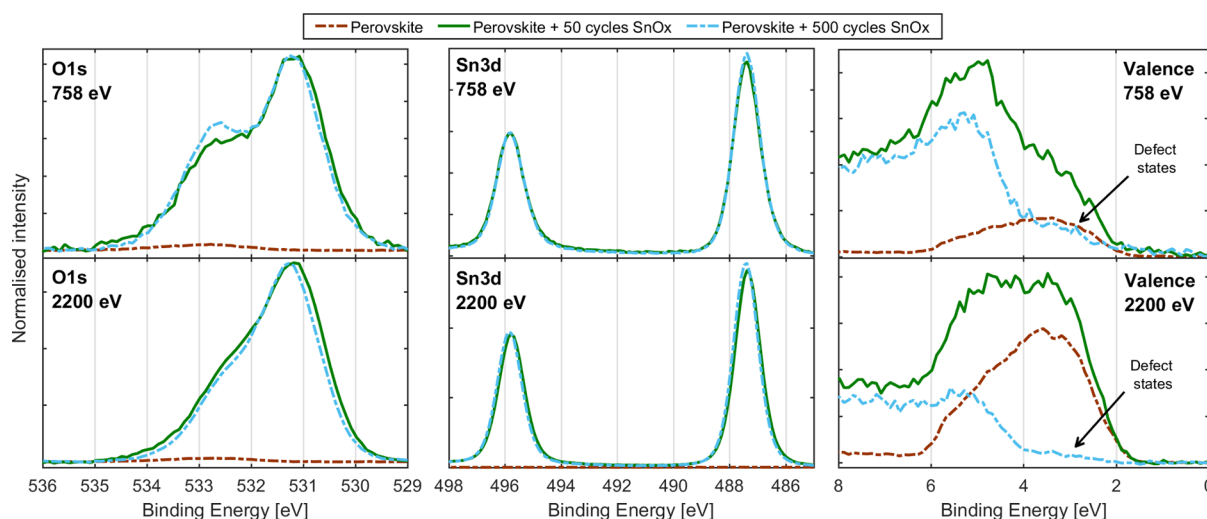


Figure 7. O 1s and Sn 3d core levels and the valence band measured with a photon energy of 758 and 2200 eV. Intensities are normalized to I 4d for the perovskite and Sn 3d total area for the SnO_x reference. The binding energy is calibrated against Au 4f_{7/2} at 84 eV.

grow on a more pristine perovskite film that has lost less mass prior to deposition. The mass dynamics show that it takes fewer cycles to reach the saturated growth regime, resembling the dynamics at 60 °C mentioned above. Perhaps, this is related to the sample not being able to reach 90 °C during the short preheating time prior to deposition. A starting SnO_x CVD step was also introduced to see if the suspected reaction between the perovskite surface and TDMASn mentioned above could be prevented by simultaneously providing H₂O into the reactor. This should facilitate a competing reaction where TDMASn reacts with H₂O to form SnO_x and H–DMA. During the CVD step, the mass increases rapidly without any visible inhibition, as shown in Figure 5b. The ALD growth that follows approximately 30 s later immediately shows a saturated mass gain per cycle.

2.3. Photoelectron Spectroscopy. Figures 6 and 7 show the core-level spectra of Pb 4f, I 4d, Br 3d, N 1s, O 1s, and Sn 3d and the valence band spectra for the bare perovskite sample, the sample with 50 cycles of ALD SnO_x at 90 °C on the

perovskite, and the sample with 500 cycles of ALD SnO_x at 90 °C on the perovskite. Additional data (C 1s, Cs 4d, and Pb 5d core-level spectra) are shown in the Supporting Information (see Figure S4). Each sample is measured with SOXPES and HAXPES using photon energies of 758 and 2200 eV, respectively. The different photon energies enable an escape depth for the electrons of about 4.5 nm for SOXPES and about 8 nm for HAXPES according to the universal curve for the inelastic mean free path.³⁵ Although these escape depths do not account for the differences in kinetic energies of electrons escaping from different core levels, they give a good approximation for the lower binding energy core levels Pb 4f, Br 3d, and I 4d and an upper limit for the higher binding energy core levels N 1s, O 1s, and Sn 3d. The SnO_x/perovskite N 1s, Pb 4f, Br 3d, and I 4d core levels were analyzed by comparing with the bare perovskite. The curve-fit procedure is described in the Experimental Methods section and shown in Figures S5 and S6 in the Supporting Information. The positions of the new interfacial components in relation to

the bare perovskite for the sample with 50 cycles of ALD are shown in Figure 6.

2.3.1. Uncoated Perovskite. For both SOXPES and HAXPES, the binding energies and element/Pb ratios of Pb 5d, I 4d, Br 3d, and N 1s (see Table S2 in Supporting Information) for the uncoated perovskite resemble previously measured perovskite films that were made in-house using a similar deposition process.³⁶ In Figure 6, the N 1s signal shows the presence of an FA⁺ signal at 400.9 eV and small MA⁺ signal at 402.4 eV.³⁷ The MA/FA ratio of about 1:10 (see Table S2 in the Supporting Information) also corresponds well with the measured value in the previous in-house study.³⁶

2.3.2. Perovskite after 500 Cycles of SnO_x. After 500 cycles of ALD SnO_x at 90 °C on the perovskite, the ALD reached the steady-state growth per cycle, as shown in the QCM data above, and an approximately 50 nm thick closed SnO_x layer is formed on the perovskite surface.¹⁷ Thus, the photoelectron spectra from both SOXPES and HAXPES for the sample with 500 cycles of SnO_x ALD on the perovskite will give information about the bulk of the SnO_x film. As expected, both Sn and O have strong signals for this sample, whereas no traces of I 4d and Pb 5d doublets from the perovskite are found (Figures 6 and S2, respectively). However, a weak Br 3d doublet (Br 3d_{5/2} at 69.5 eV and Br 3d_{3/2} at 70.4 eV) at a higher binding energy than the perovskite can be detected (see the Discussion section below). Sn 3d in Figure 7 shows a single symmetric doublet (Sn 3d_{5/2} at 487.4 eV and Sn 3d_{3/2} at 495.8 eV) that most likely originates from the Sn⁴⁺ state in a SnO_x compound, which is also found when SnO_x is deposited on glass (Figure S8 in the Supporting Information). Although the peak position of the strongest O 1s contribution at 531.2 eV, shown in Figure 7, suggests a metal oxide, there is an additional higher binding energy contribution at 532.6 eV that most likely relates to a metal hydroxide or metal carbonate.³⁸ The higher binding energy contribution is also more pronounced for SOXPES than for HAXPES, indicating that it is more prevalent at the surface than the SnO_x bulk. Furthermore, the O 1s signal is similar to that observed when SnO_x is deposited on glass (Figure S8 in the Supporting Information). There are signals of N both in SOXPES and HAXPES with similar N/Sn atomic ratios (Table S2 in the Supporting Information). This indicates that N does not only stem from surface contamination but must be present within the SnO_x film, which is further reinforced by the observation of a N signal even when SnO_x is deposited on glass (Figure S9 in the Supporting Information). This agrees with previous studies that have measured the presence of N or the presence of DMA ligands in the SnO_x film.^{38,39} Analyzing the N 1s signal in Figure 6 in more detail, it is apparent that it is not a single peak as it extends in binding energy from 399 to 403 eV. Not only does this binding energy range include the energies that correspond to FA and MA environments within the perovskite but it also extends to lower energies showing the presence of a more reduced nitrogen species. The N 1s spectrum looks similar when SnO_x is deposited on glass without the presence of the perovskite (Supporting Information Figure S9). Thus, although it is still possible that MA or FA is present in the SnO_x film through exchange reactions with DMA when it is grown on perovskite,¹⁸ it seems likelier that the N state originate from DMA with parts of it being trapped within the film during the growth.³⁹

2.3.3. Perovskite after 50 Cycles of SnO_x. For the sample with 50 cycles of ALD at 90 °C on the perovskite, the ALD

process should just have reached a steady growth rate per cycle based on the data from QCM measurements. Thus, the growth is terminated just after the perovskite/SnO_x interface formation is complete. Measuring this sample with SOXPES should therefore mainly sample the perovskite/SnO_x interface, whereas HAXPES will reach deeper, probing the perovskite material beneath the interface. By analyzing the resulting spectra from both SOXPES and HAXPES, it is thus possible to obtain insights into the chemical environments at the interface, the integrity of the perovskite material beneath, and to obtain a rough estimate of the interface layer thickness. The SOXPES and HAXPES spectra for O 1s and Sn 3d are very similar to those of the 500 cycles of SnO_x on the perovskite sample, as shown in Figure 7. Sn 3d is symmetrical and has the same peak position, indicating Sn⁴⁺ in an oxygen environment. O 1s still has two contributions, one from pure Sn⁴⁺ oxide at 531.2 eV and a higher binding energy contribution that is possibly from Sn hydroxide or Sn carbonate at 532.6 eV. Figure 6 shows an I 4d doublet (I 4d_{5/2} at 49.5 eV and I 4d_{3/2} at 51.2 eV) which corresponds well to the uncoated perovskite. However, some additional broadening is observed in the SOXPES spectra, which could be either due to the new chemical species or just increased disorder at the interface. Figure 6, normalized to I 4d intensity, also shows an excess of Pb, Br, and N compared to the uncoated perovskite sample, which is significantly greater at the interface (SOXPES) than the bulk (HAXPES). This excess appears to be due to the formation of new chemical species as their binding energy differs from that of the uncoated perovskite. As such, the interface is enriched in new Pb, Br, and N species but deficient in I. Just as for the 500 cycles on the perovskite sample, the N 1s signal spans a large range of binding energies, as illustrated in Figure 6. In contrast to the 500 cycles, there is a distinct signal at 400.9 eV originating from the perovskite and a significant signal from the more reduced nitrogen at 399.6 eV that possibly originates from metal–N.⁴⁰ Furthermore, the reduced nitrogen contribution is found to be stronger for SOXPES than for HAXPES for this sample. From this, it is apparent that the reduced N 1s contribution is over-represented at the interface compared to the SnO_x bulk and that it does not seem to exist to the same extent, if at all, in the perovskite bulk. The Br 3d spectrum (Figure 6) shows the formation of a new bromine doublet that is at a higher binding energy than the perovskite doublet (Br 3d_{5/2} at 68.8 eV and Br 3d_{3/2} 69.7 eV). This new species stems mainly from the interface region as it is stronger compared to the perovskite contribution in SOXPES than in HAXPES. The higher binding energy matches the formation of Sn–Br oxides, that is, Br in an oxygen-rich surrounding, observed in MASnBr₃ perovskites upon air exposure.⁴¹ This assignment is supported by the detection of the same Br signal in the 500-cycle SnO_x film for which no perovskite signals were detected. Since the submission of our paper, another study on the interface of perovskites with oxides deposited by ALD has been published.²² The X-ray photoelectron spectroscopy (XPS) analysis of this paper shows core-level features similar to our spectra in the analysis of a perovskite/SnO_x interface, with the observation of new bromine, lead, and nitrogen species. However, in this recent study, the new Br feature is assigned to the formation of Br₂ at the interface. In our experiments, we do not expect to observe features related to Br₂, as Br₂ would be expected to either evaporate or react with its surroundings either during the ALD deposition at 90 °C or during PES under ultrahigh vacuum. The Pb 4f signal shows

the formation of a new Pb 4f doublet (Pb 4f_{7/2} at 139.3 eV and Pb 4f_{5/2} at 144.1 eV) that is not present in the uncoated perovskite (Pb 4f_{7/2} at 138.7 eV and Pb 4f_{5/2} at 143.6 eV), as seen in Figure 6. This contribution could be related to the formation of lead oxides, similar to what has been previously seen in PbS quantum dots,^{42,43} and it is stronger for SOXPES compared to HAXPES in relation to the perovskite contribution. Thus, the new Pb 4f component at higher binding energies is most prevalent at the perovskite/SnO_x interface. Additionally, the new Pb 4f component could also be related to PbBr₂, as was recently suggested.²² We note that we have observed that the binding energy difference between Pb 4f_{7/2} and Br 3d_{5/2} is about 0.3–0.4 eV larger for PbBr₂ than for mixed halide perovskites⁴⁴ and not 0.6 eV as observed here. This suggests that the formation of lead–oxygen bonds at least contributes to the new Pb 4f feature. To summarize the analysis, the interface contains a SnO_x compound with significant Br and nitrogen contamination as well as lead oxide but appears to have an iodine deficiency. Below the interfacial layer, the perovskite appears relatively intact, which agrees with only perovskite peaks appearing in X-ray diffraction (XRD) after a direct SnO_x exposure (see Figure S10 in the Supporting Information) and the intact perovskite seen in scanning tunneling electron microscopy (STEM) high-angle annular dark-field (HAADF) beneath the interface (see Figure S11 in the Supporting Information). It is not straightforward to extract the mixed interface layer thickness between the perovskite and SnO_x because of the complex environment, but assuming all iodide signals originate from the perovskite, a rough estimation would put it to be around 2–5 nm (see Table S3 and eq S1 in the Supporting Information), which also agrees decently with the not so distinct interface seen in STEM HAADF (see Figure S11 in the Supporting Information) on top of the perovskite.

2.4. Current Density–Voltage Characterization of p–i–n Solar Cells. To investigate the quality of the interface formed between the perovskite and the SnO_x p–i–n solar cells with 75 ALD cycles of SnO_x deposited directly on the perovskite as the ETL was prepared. In all of the cases where the film is directly deposited on the perovskite, the performance is low because of the low open-circuit voltage (V_{oc}), low short-circuit current density (J_{sc}), and low fill factor (FF), as seen in Figure 8a and Table 1. The low performance stems from a strong bias dependence on the light-generated current. This holds true at 90 °C even for the cases where the ALD process is started early after only 120 s of heating and for the process which uses a CVD start after 1800 s. Even the cells where the SnO_x process is performed at 60 °C, where no mass loss was seen in the QCM crystal prior to ALD, show the same poor performance. In contrast, when depositing a 10 nm thick PCBM layer on the perovskite before the ALD process, we obtain high V_{oc} , high J_{sc} , and high FF for all of the cells with SnO_x deposited at 90 °C, regardless of the initial starting conditions, as shown in Figure 8b and Table 1. The increased performance is clearly observed in the JV measurements as well, where the light-generated current is only weakly bias-dependent and the curvature resembles that of a single solar cell diode. However, the cells with PCBM and SnO_x deposited at 60 °C have a lower V_{oc} and lower FF compared to their 90 °C counterparts because of a double diode-like behavior. It is possible that this is due to the changes in SnO_x properties, such as band gap and film density, which have previously been found to change with the growth temperature.^{29,34,38} Finally,

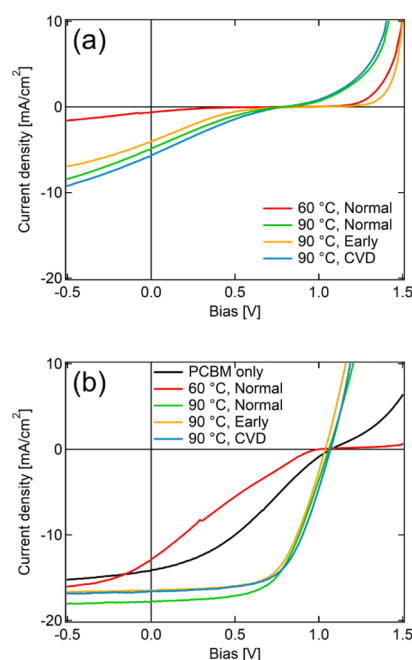


Figure 8. J – V measurements of p–i–n perovskite solar cells where the 75 SnO_x cycles are performed using different growth conditions on (a) bare and (b) 10 nm of PCBM-coated perovskite. For reference, a sample with only 10 nm PCBM and no ALD SnO_x is also shown in (b).

the reference sample with just PCBM and no SnO_x shows acceptable V_{oc} and J_{sc} but has low FF from a double diode-like behavior, possibly because of the ZnO/Al sputter process damaging the PCBM and the perovskite beneath.

3. DISCUSSION

The lower V_{oc} for all of the p–i–n solar cells without PCBM and the higher saturation current density seen in the dark JV comparison (Figure S12 in the Supporting Information) suggest that there is an increased recombination as a result of the direct ALD deposition.^{45,46} This agrees well with the lower V_{oc} observed in a previous study under similar conditions.¹⁸ It would not be unreasonable to assume that the increased recombination measured for the cells without PCBM is due to the chemically deteriorated interface observed in PES as this is the only change made between the two stacks. Furthermore, there is also a broadening toward lower energy of the valence band spectra, as shown in Figure 6. A similar observation was made in a parallel study and was suggested to be due to the midgap states within the SnO_x band gap that effectively lower the hole barrier at the interface and thereby increase interface recombination.²² A more detailed view regarding the origin of the recombination could perhaps be achieved through temperature-dependent JV in future studies.⁴⁷ The series resistance of the solar cells in this study was estimated using a basic linear fit at high positive current densities for both the light and the dark JV curves shown in Figures 8 and S12. The values are similar for the cells with or without PCBM and follows no consistent trend, as suggested by the parallel study.²² However, the model is basic, and a more in-depth analysis at even higher current densities would be beneficial for further understanding.^{45,46} All of the p–i–n perovskite devices where SnO_x is deposited directly on Cs_{0.05}FA_{0.79}MA_{0.16}PbBr_{0.51}I_{2.49} show a severe bias dependence

Table 1. Resulting Performance for p–i–n Perovskite Solar Cells Using 75 SnO_x ALD Cycles at Different Conditions and with Different Interlayer Stacks^a

ALD temp. [°C]	ALD start	PCBM	V _{oc} [V]	J _{sc} [mA/cm ²]	FF [%]	efficiency [%]
60	normal	no	0.67 ± 0.05	0.4 ± 0.1 (0.7)	16.7 ± 2.0	0.0 ± 0.0 (0.1)
60	normal	yes	0.98 ± 0.04	11.7 ± 1.3 (16.9)	21.3 ± 1.2	2.4 ± 0.3 (3.5)
90	normal	no	0.69 ± 0.08	4.1 ± 1.3 (6.3)	18.8 ± 0.8	0.5 ± 0.3 (0.8)
90	normal	yes	1.07 ± 0.02	17.6 ± 0.4 (17.9)	55.5 ± 3.1	10.4 ± 0.5 (10.6)
90	early	no	0.63 ± 0.16	2.5 ± 0.7 (5.1)	14.9 ± 2.0	0.2 ± 0.1 (0.5)
90	early	yes	1.03 ± 0.04	16.3 ± 0.6 (17.6)	55.9 ± 4.3	9.4 ± 0.8 (10.1)
90	CVD	no	0.61 ± 0.14	3.0 ± 1.4 (5.2)	20.3 ± 2.3	0.4 ± 0.3 (0.6)
90	CVD	yes	1.09 ± 0.02	16.7 ± 0.6 (17.8)	57.8 ± 3.5	10.5 ± 0.7 (11.2)
PCBM only		yes	1.07 ± 0.02	14.5 ± 0.9 (16.8)	31.8 ± 2.8	5.0 ± 0.7 (5.7)
p–i–n reference			1.12 ± 0.01	18.1 ± 1.7	66.1 ± 5.1	13.5 ± 1.8

^aData for p–i–n reference cells using the same perovskite solution are also included for comparison. Values are listed as: average ± standard deviation. The J_{sc} value from the quantum efficiency measurement of a representative cell and the resulting rescaled efficiency are shown in parenthesis.

of the light-generated current. This curvature is not present in the dark measurement of a representative device, as shown in Figure S12 in the [Supporting Information](#), indicating that the bias dependence is related to the light-generated current only. In stark contrast, if the same SnO_x process is used but the perovskite is first protected by a thin PCBM film, the bias dependence of the light-generated current is not present, and a more ideal single solar cell diode curvature is seen in *JV*. The corresponding dark curve of a representative solar cell using PCBM shows dynamics very similar to the one without (see Figure S12 in the [Supporting Information](#)), indicating that the diffusion current is almost unaffected by the inclusion of PCBM. As there is no bias dependence of the light current for the device with PCBM, thermionic emission must be enough for the photogenerated carriers to cross all of the interfaces on their way to the contacts.^{45,46} This is evidently not the case for the devices without PCBM. As only the electron-selective contact has been changed by using or not using PCBM, the issue of bias-dependent transport must be due to a limited transport for light-excited electrons across the perovskite/SnO_x interface. This heavily implies that an energy barrier is present for the electrons as seen from the perovskite at the perovskite/SnO_x interface, as was previously reported for both (MA,FA)-Pb(Br,I)₃ and (Cs,FA)Pb(Br,I)₃.^{15,16} Furthermore, from the n–i–p devices where a SnO_x/perovskite interface is used, it is observed that there is no bias dependence, as shown in Figure S14 in the [Supporting Information](#), indicating that there is no barrier and that thermionic emission is enough to cross the interface. It also implies that there is nothing intrinsically wrong with the SnO_x and perovskite band alignments from our processes. Thus, the barrier only appears when the perovskite is directly exposed to the ALD process. The nature of the barrier could be due to the introduction of a positive conduction band offset, as seen from the perovskite as previously suggested,^{17,18} or due to an upward band bending of the perovskite conduction band toward the interface. The latter could perhaps be the result of either the charge accumulation or the interface dipole that was observed in a parallel study of this interface.²² It is also worth noting that the cell with PCBM and an ALD process at 60 °C still shows a bias-dependent light-generated current. From the in-house experiments and previous studies regarding the same or similar ALD chemistries, the band gap of SnO_x is found to increase with a decreasing ALD deposition temperature.^{29,34,38} It is therefore not unreasonable that for a low enough ALD

deposition temperature, the bulk band gap of SnO_x increases enough to create an energy barrier by itself in the conduction band, as seen from the perovskite.

The QCM data give some interesting insights into the formation of the barrier from the initial growth dynamics of the SnO_x ALD on the perovskite film. At temperatures of 90 and 120 °C, the perovskite is found to lose mass during the preheating at 4 Torr in N₂ gas prior to the ALD process. It is not unreasonable that the mass loss relates to the thermal decomposition of the perovskite forming gaseous reaction products such as, for example, MAI and I₂ that leave the perovskite film at the surface,^{48,49} especially when considering the decreased amount of I found by PES at the perovskite/SnO_x interface. Thus, at 90 and 120 °C, the possibility to form an ideal perovskite/SnO_x interface is potentially lost already prior to the ALD. Trying to mitigate this effect by using a lower growth temperature of 60 °C and starting the process at 90 °C after a very short preheating did, however, not improve the solar cell performance, suggesting that the barrier formation is related to the direct exposure of ALD precursors or the process itself. It is somewhat surprising that no mass was lost during the H₂O exposure of the perovskite surface as it typically facilitates its decomposition into heavier gaseous MAI and solid PbI₂, but this process has also been found to be dependent on time and H₂O pressure, where a low vapor pressure over a short time is typically not detrimental.^{50–52} As an example, a previous study found an increase in mass when pulsing H₂O vapor over MAPbI₃ at 75 °C,¹² where the conclusion was that the amount of H₂O was not enough to induce the decomposition and that H₂O would therefore hydrate the perovskite instead. In this study, the resulting partial pressure of H₂O vapor from the precursor bottle at room temperature that is further reduced using a needle valve was perhaps therefore not high enough to distinctly change the mass loss rate that already appears by heating the perovskite at 90 °C. Not even during extended H₂O exposures, as shown in Figure S3 in the [Supporting Information](#), was there a deviation in mass loss rate. The quick and persistent mass gain from the TDMASn pulse exposure, however, suggests that the added mass during the pulse was a spontaneous and continuous reaction between the precursor and the perovskite surface (Figure S3 in the [Supporting Information](#)). A similar result was also shown in a previous study, where a modified surface was found in conjunction with a mass gain during the low partial pressure TMAI exposures of perovskite.¹³ The initial exposure

of TDMASn during the ALD processes in this study was found to leave a surface that gave a smaller mass gain for the following SnO_x cycles as compared to the film-on-film growth regime. Thus, after the initial exposure of TDMASn, there seems to be less-than-expected –DMA ligands at the surface, which would reduce the number of sites that H_2O can react with and in turn would limit the amount of –OH groups that TDMASn can react with in the next pulse, effectively reducing the mass gain per cycle. One plausible explanation for the surface-inhibited growth is that the surface is initially poisoned by Br, released from the perovskite, and later found in the SnO_x film by the PES measurements. Poisoning by halogen impurities at lower deposition temperatures is common in ALD because of the fact that halide precursors generally require higher deposition temperatures to drive the growth reaction. This is also true for the growth of SnO_x by using the $\text{SnCl}_4/\text{H}_2\text{O}$ and $\text{SnI}_4/\text{H}_2\text{O}$ precursor combinations. From the CVD start process, the growth of SnO_x seems to happen without delay, but the solar cells using this start showed the same barrier-inhibited performance as those with a regular ALD process. This indicates that TDMASn still reacts with the perovskite surface initially or in parallel to the reaction with H_2O during CVD.

Figure 9 shows the perovskite/ SnO_x interface chemistry based on the PES measurements. This complex interfacial

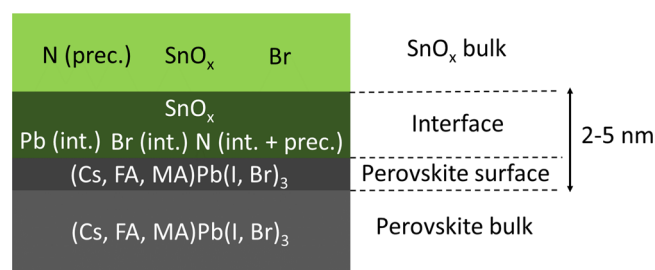


Figure 9. Schematic of the perovskite/ SnO_x interface chemistry based on SOXPES and HAXPES analyses.

environment suggests that there is a strong interaction between the TDMASn precursor and the perovskite surface, which was also shown by QCM measurements. Although their origin is not certain, a few reactions seem plausible. As Sn has a strong affinity to Br, the formation of Br–Sn bonds because of TDMASn adsorption could weaken the Pb–Br bonds of the perovskite surface, which, after SnO_x formation, could explain the new Br and Pb signals at the interface. The interfacial Pb signal could then relate to the formation of Pb–O bonds, created during subsequent water pulses, especially where Pb–Br bonds were broken during the initial TDMASn exposure. The presence of Br in the SnO_x bulk also strongly indicates that bonds have been broken at the perovskite surface during TDMASn exposure. Furthermore, we find the expected N signals of FA and MA in the perovskite and a broader peak presumably related to the incorporation of, or decomposed parts of, DMA, MA, or FA in SnO_x .^{38,39} If we consider the nitrogen signal in detail, we see that DMA and MA should provide similar binding energies, whereas FA is at a lower binding energy. Interestingly, there is an additional nitrogen species at binding energies lower than that of FA, concentrated at the interface that could be related to a metal–N bond.⁴⁰ As the N signal is fairly broad for the SnO_x bulk, even when it is grown on glass, it is not unreasonable that this lowest binding

energy N species is present in the SnO_x bulk already because of the previously mentioned decomposition of DMA during growth. Curiously, this species is enriched at the perovskite/ SnO_x interface compared to that in the SnO_x bulk, suggesting that the initial reaction with the perovskite promotes the formation of this species, potentially through a reaction with the organic cation. The I deficiency at the interface could, as previously discussed, be a result of the perovskite decomposing during the ALD preheating, releasing gaseous reaction products such as I_2 or MAI. A previous study also suggested that I in the form of I_2 could leave the perovskite surface as a by-product from an exchange reaction between DMA of the TDMASn precursor and FA of the perovskite surface.¹⁸ Judging by the substantial mass loss seen prior to deposition in QCM crystals for temperatures 90 and 120 °C, the former seems likely. The initial ALD dynamics are however similar at all deposition temperatures, which suggests that the surface reaction is not dependent on temperature and on potential mass loss from the perovskite surface. Based on this analysis, there are a few options on what causes the transport barrier for the p–i–n solar cells with direct perovskite/ SnO_x interfaces. Considering that previous studies have found an increasing band gap of ALD SnO_x when there is an increased amount of C, N, and OH impurities in the film, it is plausible that the SnO_x band gap at the interface in this study increases as well as there is even more N and significant amount of Br there.^{29,38} Although an increased band gap does not necessarily shift the conduction band level up enough to prevent the transfer of the excited electrons from the perovskite, it is not unreasonable to think that it could. From the PES data, it is observed that the formation of PbO is also possible at the interface, which would create a small barrier as the conduction band of PbO is expected to be at a slightly higher energy than that of pure SnO_2 .⁵³ The PES data also show that the interface layer clearly contains new Pb, Br, and N species, indicating that the top of the perovskite becomes degraded during the ALD exposure. If so, the degraded perovskite could potentially introduce a different Fermi-level pinning at the perovskite/ SnO_x interface of the p–i–n solar cells compared to the working SnO_x /perovskite interface of the n–i–p solar cells and in the worst-case scenario force the bands to bend upward in the perovskite toward the perovskite/ SnO_x interface. This would accumulate charge carriers and possibly shift the vacuum energy level, which were the observations made in a parallel study.⁷² Either of the barrier options are valid by themselves, but it cannot be excluded that they are also present at the same time as the perovskite surface, the interface, and the SnO_x film all have been altered.

Looking forward, the most important issue that needs to be solved for ALD chemistries on perovskite surfaces is to prevent unwanted surface reactions during the initial precursor exposures of the bare perovskite. This could be achieved by changing the perovskite composition to something inorganic that has a higher heat tolerance, such as, for example, CsPbBr_3 ,⁵⁴ which would limit the amount of possible reactions prior to and during the SnO_x ALD exposure. However, even a small compositional change as increasing the Br concentration of $(\text{Cs,FA})\text{Pb}(\text{Br,I})_3$ to increase the moisture stability and thereby the stability to the ALD process has, in a previous study, shown to improve the interface quality.¹⁸ A more promising route could be to design new ALD precursor chemistries that allow for film growth on perovskite surfaces without unwanted interface reactions. Earlier studies hinted

that high-reactivity ligands such as DMA, alkyls, and alkoxides caused detrimental damage to the perovskite.^{11–21} However, in a parallel study, the DMA ligand was used to deposit both SnO_x and TiO_2 with H_2O as the counter reactant, and the $(\text{Cs,FA})\text{Pb}(\text{Br,I})_3/\text{TiO}_2$ interface became more pristine than the deteriorated $(\text{Cs,FA})\text{Pb}(\text{Br,I})_3/\text{SnO}_x$ interface that showed a similar chemistry as in this study.²² Thus, both the metal center and the ligand clearly need to be taken into account when designing new precursors for ALD on perovskites. Although the task of finding a solution to the interface problem seems daunting, there are a lot of options left to try, considering that the perovskite composition, the ALD process, the Sn precursor, and the O precursor can all be changed into already existing or newly developed alternatives.

4. CONCLUSIONS

ALD of SnO_x directly onto $\text{Cs}_{0.05}\text{FA}_{0.79}\text{MA}_{0.16}\text{PbBr}_{0.51}\text{I}_{2.49}$ led to poor p–i–n solar cell performance because of an electron transport barrier. In contrast, good performance was achieved for the same ALD SnO_x when the surface is protected by PCBM in p–i–n solar cells and when an n–i–p solar cell stack was used where the perovskite is deposited onto SnO_x instead. To investigate what happens during the direct ALD growth on the perovskite, PES and QCM measurements were employed. From the QCM measurements, two main results related to the interface formation were observed. First, the growth appears to be nucleation-limited with a slower initial growth per cycle that eventually picks up to a saturated film-on-film value after 20–50 cycles depending on the temperature and perovskite composition. There is one important exception to this as the quick and irreversible mass gain during the first TDMA Sn pulse is similar to the later film-on-film growth but without a corresponding film-on-film loss during the following H_2O pulse. As this is observed for all the samples, even the ones at 60 °C where no mass loss is observed prior to ALD, it suggests that TDMA Sn spontaneously reacts with the perovskite surface to form the interface layer. Second, there is a slow mass loss over time during the ALD preheating in a low vacuum for 90 and 120 °C, but not for 60 °C, possibly indicating that the perovskite decomposes prior to deposition. From PES, it is observed that the perovskite/ SnO_x interface is found to be deficient in I and contains new species of Pb, Br, and N in addition to the expected perovskite signals and SnO_x signals. This further suggests that there is an unwanted reaction between the perovskite and the precursors of the ALD process. Furthermore, the new species originate from an interfacial layer of a few nanometers on top of the bulk perovskite. Based on this analysis, the interfacial layer with its nonideal composition is suggested to be the reason for the electron transport barrier.

5. EXPERIMENTAL METHODS

5.1. General Layer Synthesis. The FTO substrates were cleaned using Hellmanex and a toothbrush and thereafter ultrasonicated for 30 min in a Hellmanex bath, followed by an ethanol bath and an acetone bath. Perovskite precursor solutions were prepared in a glovebox in argon atmosphere. Stock solutions of PbI_2 and PbBr_2 were prepared in advance, whereas the final precursor solutions were prepared just before perovskite deposition. Anhydrous *N,N*-dimethylformamide/dimethyl sulfoxide (DMSO) in the proportion of 4:1 was used as the solvent. The PbI_2 and PbBr_2 solutions were close to the saturation point, and to ensure that the lead salts are completely dissolved, the solutions were heated under stirring using a hotplate set at approximately 100 °C for 20 min and then cooled down to room temperature just before use. Two different perovskite compositions

were explored: (1) $\text{Cs}_{0.05}\text{FA}_{0.79}\text{MA}_{0.16}\text{PbBr}_{0.51}\text{I}_{2.49}$ (normal perovskite) and (2) $\text{Cs}_{0.17}\text{FA}_{0.83}\text{PbBr}_{0.51}\text{I}_{2.49}$ (without MA perovskite), where MA is methylamine, CH_3NH_2 , and FA is formamidinium, $\text{CH}(\text{NH}_2)_2$. For (1), two master solutions were prepared (a) 1.25 M PbI_2 and 1.14 M FAI and (b) 1.25 M PbBr_2 and 1.14 M MABr. These were mixed in the proportion $a/b = 83:17$. To this solution, 5% (by volume) of 1.38 M CsI in DMSO was added. The solutions for (2) needed to be carefully prepared because of the lower solubility of CsI. In this case, three master solutions were prepared: (a) 1.25 M PbI_2 and 1.125 M FAI, (b) 1.25 M PbBr_2 and 1.125 M MABr, and (c) 1.25 M PbI_2 and 1.125 M CsI. These were mixed in the proportion $a/b/c = 66:17:17$. CsI does not dissolve properly, wherefore solutions (a) and (b) were poured into (c) in the right proportion. The MA and FA salts were bought from Dyesol, the lead salts from TCI, solvents from Fisher, and the remaining chemicals from Sigma-Aldrich. All chemicals were used as received without further treatment. The perovskites were spin-coated in a nitrogen-filled glovebox. For each sample, with the dimensions of $1.4 \times 2.4 \text{ cm}^2$, 35 μL of the precursor solution was spread over the substrate, which thereafter was spin-coated using a two-step program. The first step was a spreading step using a rotation speed of 1000 rpm with an acceleration of 200 rpm/s for 10 s. This step was immediately, without pause, followed by the second step where the films were spun at 6000 rpm for 20 s using an acceleration of 2000 rpm/s. During the second step, when approximately 5 s of the program remains, 100 μL of anhydrous chlorobenzene was applied on the spinning film with a handheld automatic pipette. NiO_x films were deposited on cleaned FTO by reactive pulsed DC sputtering at 500 W from a metallic Ni target. The gas flows into the chamber were 25 sccm of O_2 and 25 sccm of Ar, and the resulting pressure was regulated to be 6×10^{-3} Torr. The deposition time was 45 s, resulting in a $25 \pm 5 \text{ nm}$ thick film, as measured by profilometry and cross-sectional SEM. PCBM, if included, was thermally evaporated to a thickness of 10 nm from a tungsten boat in an evaporator from Leica (EM MED020) at a pressure of around 2×10^{-5} Torr and at a slow rate of 0.1 Å/s. SnO_x was deposited by thermal ALD at 60, 90, or 120 °C in an F120 Microchemistry reactor using an ALD cycle of TDMA Sn (Pegasus)/ N_2 purge/deionized (DI) $\text{H}_2\text{O}/\text{N}_2$ purge with the corresponding pulse times of 0.4/0.8/0.4/0.8 s. These pulse times were chosen as they gave an almost saturated pulse and purge dynamic at 90 and 120 °C when deposited on soda lime glass in a previous in-house study using the same ALD reactor and precursors.³³ At 60 °C, the TDMA Sn pulse did not fully saturate in 0.4 s (see Figure S2 in the Supporting Information), and the following N_2 purge also suggests that part of TDMA Sn is physisorbed as the sample loses mass during the purge. A total of 75 ALD cycles were used to grow the SnO_x layer in the p–i–n solar cells. SnO_x CVD was performed in the same F120 Microchemistry reactor by keeping the water pulse valve continuously open and then opening the valve to the TDMA Sn precursor, where the mass change seen by QCM crystals is measured. The ZnO/Al sputtering mostly followed an established baseline procedure.⁵⁵ Compared to the baseline, the RF sputter power was increased to 400 W and the time shortened to 125 s, resulting in a film thickness of $230 \pm 20 \text{ nm}$ and sheet resistance of $50 \pm 5 \Omega/\square$, as measured on glass reference pieces. To deposit Al_2O_3 , thermal ALD was performed at 200 °C in a PICOSUN R200 reactor using tri(methyl)aluminum (TMA) (EpiValence) and DI H_2O , with a TMA/ N_2 purge/DI $\text{H}_2\text{O}/\text{N}_2$ purge ALD cycle, using corresponding pulse times of 0.1/0.4/0.1/0.6 s, respectively. This ALD cycle was repeated 200 times with a saturated growth per cycle value of approximately 1 Å/cycle.

5.2. Quartz Crystal Microbalance Monitoring during ALD of SnO_x . During the SnO_x ALD process, the QCM crystals with the partial p–i–n stack, as shown in Figure 1c, were used to monitor the growth. An unpolished and AT cut quartz crystal covered by a Cr/Au metal stack was used as the substrate (Inficon, 6 MHz, 14 mm). The Al_2O_3 layer was then deposited on Au to prevent it from diffusing into or reacting with the subsequent NiO_x and perovskite materials. The NiO_x layer was used to mimic the perovskite deposition conditions of the p–i–n solar cell structure, so that the resulting perovskite was as representative as possible to the one found in the solar cells. Both the

Al₂O₃ and the NiO_x layers were deposited using a shadow mask with a circular opening in the middle that was slightly larger than the active area of the quartz crystal resonator (see Figure S16b in the [Supporting Information](#)). The shadow mask was removed before the perovskite deposition, not to disrupt the spin coating, and the result is shown in Figure S16c in the [Supporting Information](#). Afterward, the perovskite was carefully scratched away on the outer contacting area of the QCM system so that a good electrical contact with the QCM holder was still achieved. The QCM holder was previously custom-made for the F120 Microchemistry reactor to place the active QCM surface in the center of one of the reaction chamber walls, where it will be exposed to the ALD process. The QCM signal was passed through a transducer and then to an Inficon SQM 160 thin-film deposition monitor, where time versus frequency output was recorded. The frequency shift was used to estimate the mass change per area, through the Sauerbrey equation⁵⁶ (eq 1), where f_0 is the fundamental crystal resonance frequency, A is the active crystal resonator area, μ_0 is the density of quartz, and ρ_0 is the shear modulus of quartz.

$$\Delta f = -\frac{2f_0^2}{A\sqrt{\rho_0\mu_0}}\Delta m \quad (1)$$

In order to detect the effect of precursor exposure and ALD dynamics with the QCM measurements, it was necessary to determine the background signal of the measurement. Fictive mass changes in the QCM signal can be caused by variations in both temperature and pressure. The heater oscillations from the temperature regulation of the ovens were found to be small and slow enough (hours) to not be confused with the pulse signals. The change in the QCM signal because of the pump down of the system was stabilized within 120 s as the pressure drop saturated and could thus be easily separated from the pulse signals. Finally, by pulsing the precursor lines using only nitrogen carrier gas, no mass gain or loss was observed, enabling us to separate the effect of the precursor exposure and the potential pressure changes because of pulsing.

5.3. Current Density–Voltage Characterization of Solar Cells. The n–i–p cells with nontransparent metal front contacts were illuminated from the backside, that is, the FTO side. The J – V curves of the devices were measured using a home-built system. To simulate solar light, a Newport solar simulator (model 91160) with a xenon arc lamp and an AM 1.5 filter was used. The light intensity was calibrated with a silicon photodiode. The J – V curves were measured with a digital source meter (Keithley 2400). No equilibration time or light soaking was applied before the potential scan. The starting point for the measurements was chosen as 1.2 V. From this point, the potential was scanned to short circuit and back again using a scan speed of 20 mV/s. Thereafter, the dark current was sampled using the same scan speed. The cells were masked with a metal mask in order to limit the active cell area to 0.126 cm². The J – V curves of the p–i–n perovskite cells were measured in a Newport ABA solar simulator, where the light intensity was calibrated using a Hamamatsu S1337-66BR silicon photodiode to give the same short-circuit current density in the solar simulator as the photodiode has under AM 1.5 illumination. The sweep direction went from positive to negative bias at a speed of 400 mV/s, and the illumination was incident from the ZnO/Al side. No light soaking or equilibration time was applied before sweeping.

5.4. Photoelectron Spectroscopy. PES was carried out at the I09 beamline at the Diamond Light Source using SOXPES at 758 eV and HAXPES at 2200 eV; 758 eV was generated using the HUS6 undulator and monochromated using a plane grating monochromator. X-rays of 2200 eV were generated using the U27 undulator and monochromated using a Si(111) double-crystal monochromator with a secondary monochromator using back-reflecting Si(111), Si(011), and Si(001) channel cuts. The beam was defocused in order to reduce the beam damage. The photoelectrons were detected using a Scienta Omicron EW4000 HAXPES hemispherical analyzer using a pass energy of 100 eV at 758 eV and 200 eV at 2200 eV. The survey measurements were carried out using a step size of 0.5 eV and the high-resolution measurements using a step size of 0.1 eV. The measurements were calibrated against the Fermi level or Au 4f core

level at 84 eV of a grounded gold film mounted on the manipulator. The measured core levels were fitted using a pseudo-Voigt function with a polynomial, Herrera-Gomez⁵⁷ and Shirley background.⁵⁸ The intensity (peak area, $I_{A,X}$) of the species A of core level X derived by the Voigt function is proportional to the photoionization cross section⁵⁹ ($\sigma_{A,X}$) of the core level X of element A at the photon energy ($h\nu$), and the integral of atomic density (ρ_A) of that species A at depth z and the probability of escape of the emitted photoelectrons depending on the mean free path λ . This can be summarized in the following simplified eq 2.

$$I_{A,X} \propto \sigma_{A,X}(h\nu) \int_0^\infty \rho_A(z) e^{-z/\lambda(E_{kin})} dz \quad (2)$$

By assuming homogeneous materials and by dividing the cross section⁵¹ and comparing orbitals with similar binding/kinetic energies, values here referred to as relative atomic densities for the different elements and species in the perovskite samples were extracted. However, because of the exponential decrease in the escape probability of the photoelectrons in nonhomogeneous materials, neglecting the β -value correction and variations in transmission, the atomic density obtained should merely be used to follow trends when comparing different samples and give estimations than absolute values.

■ ASSOCIATED CONTENT

Supporting Information

The Supporting Information is available free of charge at <https://pubs.acs.org/doi/10.1021/acsaem.0c02405>.

Initial mass dynamics for SnO_x grown on a bare QCM monitor crystal; HAXPES and SOXPES spectra for C 1s, Cs 4d, and Pb 5d; tabulated peak positions and peak intensity relations for all of the HAXPES and SOXPES measurements; calculations of the perovskite/SnO_x interface layer thickness; XPS spectra, peak positions, and peak ratios for ALD SnO_x grown on soda lime glass (PDF)

■ AUTHOR INFORMATION

Corresponding Author

Adam Hultqvist – Department of Materials Science, Uppsala University, Uppsala 75103, Sweden; orcid.org/0000-0002-2402-5427; Email: adam.hultqvist@angstrom.uu.se

Authors

T. Jesper Jacobsson – Department of Chemistry–Ångström, Uppsala University, Uppsala 75120, Sweden; Division of Renewable Energies, Helmholtz-Centrum Berlin, Berlin 14109, Germany; orcid.org/0000-0002-4317-2879

Sebastian Svanström – Department of Physics and Astronomy, Uppsala University, Uppsala 75120, Sweden

Marika Edoff – Department of Materials Science, Uppsala University, Uppsala 75103, Sweden

Ute B. Cappel – Department of Chemistry, KTH Royal Institute of Technology, Stockholm 11428, Sweden; orcid.org/0000-0002-9432-3112

Håkan Rensmo – Department of Physics and Astronomy, Uppsala University, Uppsala 75120, Sweden

Erik M. J. Johansson – Department of Chemistry–Ångström, Uppsala University, Uppsala 75120, Sweden; orcid.org/0000-0001-9358-8277

Gerrit Boschloo – Department of Chemistry–Ångström, Uppsala University, Uppsala 75120, Sweden; orcid.org/0000-0002-8249-1469

Tobias Törndahl – Department of Materials Science, Uppsala University, Uppsala 75103, Sweden; orcid.org/0000-0001-7757-5847

Complete contact information is available at:
<https://pubs.acs.org/10.1021/acsaem.0c02405>

Notes

The authors declare no competing financial interest.

ACKNOWLEDGMENTS

The authors acknowledge STandUP for Energy, the Swedish Research Council (grant nos. VR 2018-04125, 2018-06465, and 2018-04330), the Swedish Foundation for Strategic Research (project no. RMA15-0130), the Swedish Energy Agency (grant nos. P43549-1 and 2017-004796), and the Göran Gustafsson foundation for their financial support. This work was carried out with the support of the Diamond Light Source, instrument I09 (proposal SI19067-1), and the authors thank Tien-Lie Lee and the staff at the Diamond Light Source for support during PES measurements. The research leading to this result has been supported by the project CALIPSOplus under grant agreement 730872 from the EU Framework Programme for Research and Innovation HORIZON 2020.

REFERENCES

- (1) Brenner, T. M.; Egger, D. A.; Kronik, L.; Hodes, G.; Cahen, D. Hybrid organic–inorganic perovskites: low-cost semiconductors with intriguing charge-transport properties. *Nat. Rev. Mater.* **2016**, *1*, 15007.
- (2) Dubey, A.; Adhikari, N.; Mabrouk, S.; Wu, F.; Chen, K.; Yang, S.; Qiao, Q. A strategic review on processing routes towards highly efficient perovskite solar cells. *J. Mater. Chem. A* **2018**, *6*, 2406–2431.
- (3) National Renewable Energy Laboratory. Best Research-Cell Efficiency Chart. <https://www.nrel.gov/pv/assets/pdfs/best-research-cell-efficiencies.20200708.pdf> (accessed July 29, 2020).
- (4) Wang, Q.; Phung, N.; Di Girolamo, D.; Vivo, P.; Abate, A. Enhancement in lifespan of halide perovskite solar cells. *Energy Environ. Sci.* **2019**, *12*, 865–886.
- (5) Rolston, N.; Watson, B. L.; Bailie, C. D.; McGehee, M. D.; Bastos, J. P.; Gehlhaar, R.; Kim, J.-E.; Vak, D.; Mallajosyula, A. T.; Gupta, G.; Mohite, A. D.; Dauskardt, R. H. Mechanical integrity of solution-processed perovskite solar cells. *Extreme Mech. Lett.* **2016**, *9*, 353–358.
- (6) Song, Z.; McElvany, C. L.; Phillips, A. B.; Celik, I.; Krantz, P. W.; Wathage, S. C.; Liyanage, G. K.; Apul, D.; Heben, M. J. A technoeconomic analysis of perovskite solar module manufacturing with low-cost materials and techniques. *Energy Environ. Sci.* **2017**, *10*, 1297.
- (7) Zhao, P.; Kim, B. J.; Jung, H. S. Passivation in perovskite solar cells: A review. *Mater. Today Energy* **2018**, *7*, 267–286.
- (8) Calió, L.; Kazim, S.; Grätzel, M.; Ahmad, S. Hole-Transport Materials for Perovskite Solar Cells. *Angew. Chem., Int. Ed.* **2016**, *55*, 14522–14545.
- (9) Meng, L.; You, J.; Guo, T.-F.; Yang, Y. Recent Advances in the Inverted Planar Structure of Perovskite Solar Cells. *Acc. Chem. Res.* **2016**, *49*, 155–165.
- (10) Yang, G.; Tao, H.; Qin, P.; Ke, W.; Fang, G. Recent progress in electron transport layers for efficient perovskite solar cells. *J. Mater. Chem. A* **2016**, *4*, 3970–3990.
- (11) Raiford, J. A.; Belisle, R. A.; Bush, K. A.; Prasanna, R.; Palmstrom, A. F.; McGehee, M. D.; Bent, S. F. Atomic layer deposition of vanadium oxide to reduce parasitic absorption and improve stability in n–i–p perovskite solar cells for tandems. *Sustainable Energy Fuels* **2019**, *3*, 1517–1525.
- (12) Choudhury, D.; Rajaraman, G.; Sarkar, S. K. Self limiting atomic layer deposition of Al₂O₃ on perovskite surfaces: a reality? *Nanoscale* **2016**, *8*, 7459–7465.
- (13) Yu, X.; Yan, H.; Peng, Q. Reaction Temperature and Partial Pressure Induced Etching of Methylammonium Lead Iodide Perovskite by Trimethylaluminum. *Langmuir* **2019**, *35*, 6522–6531.
- (14) Kim, I. S.; Martinson, A. B. F. Stabilizing hybrid perovskites against moisture and temperature via non-hydrolytic atomic layer deposited overlayers. *J. Mater. Chem. A* **2015**, *3*, 20092–20096.
- (15) Zardetto, V.; Williams, B. L.; Perrotta, A.; Di Giacomo, F.; Verheijen, M. A.; Andriessen, R.; Kessels, W. M. M.; Creatore, M. Atomic layer deposition for perovskite solar cells: research status, opportunities and challenges. *Sustainable Energy Fuels* **2017**, *1*, 30–55.
- (16) Koushik, D.; Hazendonk, L.; Zardetto, V.; Vandalon, V.; Verheijen, M. A.; Kessels, W. M. M.; Creatore, M. Chemical Analysis of the Interface between Hybrid Organic–Inorganic Perovskite and Atomic Layer Deposited Al₂O₃. *ACS Appl. Mater. Interfaces* **2019**, *11*, 5526–5535.
- (17) Hultqvist, A.; Aitola, K.; Sveinbjörnsson, K.; Saki, Z.; Larsson, F.; Törndahl, T.; Johansson, E.; Boschloo, G.; Edoff, M. Atomic Layer Deposition of Electron Selective SnO_x and ZnO Films on Mixed Halide Perovskite: Compatibility and Performance. *ACS Appl. Mater. Interfaces* **2017**, *9*, 29707–29716.
- (18) Palmstrom, A. F.; Raiford, J. A.; Prasanna, R.; Bush, K. A.; Sponseller, M.; Cheacharoen, R.; Minichetti, M. C.; Bergsman, D. S.; Leijtens, T.; Wang, H.-P.; Bulović, V.; McGehee, M. D.; Bent, S. F. Interfacial Effects of Tin Oxide Atomic Layer Deposition in Metal Halide Perovskite Photovoltaics. *Adv. Energy Mater.* **2018**, *8*, 1800591.
- (19) Seo, S.; Jeong, S.; Park, H.; Shin, H.; Park, N.-G. Atomic layer deposition for efficient and stable perovskite solar cells. *Chem. Commun.* **2019**, *55*, 2403–2416.
- (20) Brinkmann, K. O.; Gahlmann, T.; Riedl, T. Atomic Layer Deposition of Functional Layers in Planar Perovskite Solar Cells. *Sol. RRL* **2020**, *4*, 1900332.
- (21) Raiford, J. A.; Oyakhire, S. T.; Bent, S. F. Applications of atomic layer deposition and chemical vapor deposition for perovskite solar cells. *Energy Environ. Sci.* **2020**, *13*, 1997–2023.
- (22) Bracesco, A. E. A.; Burgess, C. H.; Todinova, A.; Zardetto, V.; Koushik, D.; Kessels, W. M. M.; Dogan, I.; Weijtens, C. H. L.; Veenstra, S.; Andriessen, R.; Creatore, M. The chemistry and energetics of the interface between metal halide perovskite and atomic layer deposited metal oxides. *J. Vac. Sci. Technol., A* **2020**, *38*, 063206.
- (23) Miikkulainen, V.; Leskelä, M.; Ritala, M.; Puurunen, R. Crystallinity of inorganic films grown by atomic layer deposition: Overview and general trends. *J. Appl. Phys.* **2013**, *113*, 021301.
- (24) George, S. M. Atomic Layer Deposition: An Overview. *Chem. Rev.* **2010**, *110*, 110–131.
- (25) Mackus, A. J. M.; Schneider, J. R.; MacIsaac, C.; Baker, J. G.; Bent, S. F. Synthesis of Doped, Ternary, and Quaternary Materials by Atomic Layer Deposition: A Review. *Chem. Mater.* **2019**, *31*, 1142–1183.
- (26) Kot, M.; Das, C.; Wang, Z.; Henkel, K.; Rouissi, Z.; Wojciechowski, K.; Snaith, H. J.; Schmeisser, D. Room-Temperature Atomic Layer Deposition of Al₂O₃: Impact on Efficiency, Stability and Surface Properties in Perovskite Solar Cells. *ChemSusChem* **2016**, *9*, 3401–3406.
- (27) Koushik, D.; Verhees, W. J. H.; Kuang, Y.; Veenstra, S.; Zhang, D.; Verheijen, M. A.; Creatore, M.; Schropp, R. E. I. Inline Cu(In,Ga)Se₂ High-Efficiency Humidity-Stable Planar Perovskite Solar Cells Based On Atomic Layer Architecture. *Energy Environ. Sci.* **2017**, *10*, 91–100.
- (28) Baena, J. P. C.; Steier, L.; Tress, W.; Saliba, M.; Neutzner, S.; Matsui, T.; Giordano, F.; Jacobsson, T. J.; Kandada, A. R. S.; Zakeeruddin, S. M.; Petrozza, A.; Abate, A.; Nazeeruddin, M. K.; Grätzel, M.; Hagfeldt, A. Highly efficient planar perovskite solar cells through band alignment engineering. *Energy Environ. Sci.* **2015**, *8*, 2928–2934.

- (29) Köhnen, E.; Jošt, M.; Morales-Vilches, A. B.; Tockhorn, P.; Al-Ashouri, A.; Macco, B.; Kegelmann, L.; Korte, L.; Rech, B.; Schlattmann, R.; Stannowski, B.; Albrecht, S. Highly efficient monolithic perovskite silicon tandem solar cells: analyzing the influence of current mismatch on device performance. *Sustainable Energy Fuels* **2019**, *3*, 1995–2005.
- (30) Bush, K. A.; Palmstrom, A. F.; Yu, Z. J.; Boccard, M.; Checharoen, R.; Mailoa, J. P.; McMeekin, D. P.; Hoyer, R. L. Z.; Bailie, C. D.; Leijtens, T.; Marius Peters, I.; Minichetti, M. C.; Rolston, N.; Prasanna, R.; Sofia, S.; Harwood, D.; Ma, W.; Moghadam, F.; Snaith, H. J.; Buonassisi, T.; Holman, Z. C.; Bent, S. F.; McGehee, M. D. 23.6%-efficient monolithic perovskite/silicon tandem solar cells with improved stability. *Nat. Energy* **2017**, *2*, 17009.
- (31) Lin, R.; Xiao, K.; Qin, Z.; Han, Q.; Zhang, C.; Wei, M.; Saidaminov, M. I.; Gao, Y.; Xu, J.; Xiao, M.; Li, A.; Zhu, J.; Sargent, E. H.; Tan, H. Monolithic all-perovskite tandem solar cells with 24.8% efficiency exploiting comproportionation to suppress Sn(II) oxidation in precursor ink. *Nat. Energy* **2019**, *4*, 864–873.
- (32) Al-Ashouri, A.; Magomedov, A.; Roß, M.; Jošt, M.; Talaikis, M.; Chistiakova, G.; Bertram, T.; Márquez, J. A.; Köhnen, E.; Kasparavičius, E.; Levenco, S.; Gil-Escrig, L.; Hages, C. J.; Schlattmann, R.; Rech, B.; Malinauskas, T.; Unold, T.; Kaufmann, C. A.; Korte, L.; Niaura, G.; Getautis, V.; Albrecht, S. Conformal monolayer contacts with lossless interfaces for perovskite single junction and monolithic tandem solar cells. *Energy Environ. Sci.* **2019**, *12*, 3356–3369.
- (33) Domanski, K.; Correa-Baena, J.-P.; Mine, N.; Nazeeruddin, M. K.; Abate, A.; Saliba, M.; Tress, W.; Hagfeldt, A.; Grätzel, M. Not All That Glitters Is Gold: Metal-Migration-Induced Degradation in Perovskite Solar Cells. *ACS Nano* **2016**, *10*, 6306–6314.
- (34) Lindahl, J.; Hägglund, C.; Wätjen, J. T.; Edoff, M.; Törndahl, T. The effect of substrate temperature on atomic layer deposited zinc tin oxide. *Thin Solid Films* **2015**, *586*, 82–87.
- (35) Seah, M. P. An accurate and simple universal curve for the energy-dependent electron inelastic mean free path. *Surf. Interface Anal.* **2012**, *44*, 497–503.
- (36) Jacobsson, T. J.; Svanström, S.; Andrei, V.; Rivett, J. P. H.; Kornienko, N.; Philippe, B.; Cappel, U. B.; Rensmo, H.; Deschler, F.; Boschloo, G. Extending the Compositional Space of Mixed Lead Halide Perovskites by Cs, Rb, K, and Na Doping. *J. Phys. Chem. C* **2018**, *122*, 13548–13557.
- (37) Philippe, B.; Saliba, M.; Correa-Baena, J.-P.; Cappel, U. B.; Turren-Cruz, S.-H.; Grätzel, M.; Hagfeldt, A.; Rensmo, H. Chemical Distribution of Multiple Cation (Rb⁺, Cs⁺, MA⁺, and FA⁺) Perovskite Materials by Photoelectron Spectroscopy. *Chem. Mater.* **2017**, *29*, 3589–3596.
- (38) Chistiakova, G.; Mews, M.; Wilks, R. G.; Bär, M.; Korte, L. In-situ photoelectron spectroscopy study of tin oxide layers produced from tetrakis(dimethylamino)tin by plasma enhanced atomic layer deposition. *J. Vac. Sci. Technol., A* **2018**, *36*, 02D401.
- (39) Mackus, A. J. M.; MacIsaac, C.; Kim, W.-H.; Bent, S. F. Incomplete elimination of precursor ligands during atomic layer deposition of zinc-oxide, tin-oxide, and zinc-tin-oxide. *J. Chem. Phys.* **2017**, *146*, 052802.
- (40) Ding, H.; Li, B.; Zareen, S.; Li, G.; Tu, Y.; Zhang, D.; Cao, X.; Xu, Q.; Yang, S.; Tait, S. L.; Zhu, J. In Situ Investigations of Al/Perovskite Interfacial Structures. *ACS Appl. Mater. Interfaces* **2020**, *12*, 28861–28868.
- (41) Jung, M.-C.; Raga, S. R.; Qi, Y. Properties and solar cell applications of Pb-free perovskite films formed by vapor deposition. *RSC Adv.* **2016**, *6*, 2819–2825.
- (42) Zhang, X.; Cappel, U. B.; Jia, D.; Zhou, Q.; Du, J.; Sloboda, T.; Svanström, S.; Johansson, F. O. L.; Lindblad, A.; Giangrisostomi, E.; Ovsyannikov, R.; Liu, J.; Rensmo, H.; Gardner, J. M.; Johansson, E. M. J. Probing and Controlling Surface Passivation of PbS Quantum Dot Solid for Improved Performance of Infrared Absorbing Solar Cells. *Chem. Mater.* **2019**, *31*, 4081–4091.
- (43) Miller, E. M.; Kroupa, D. M.; Zhang, J.; Schulz, P.; Marshall, A. R.; Kahn, A.; Lany, S.; Luther, J. M.; Beard, M. C.; Perkins, C. L.; van de Lagemaat, J. Revisiting the Valence and Conduction Band Size Dependence of PbS Quantum Dot Thin Films. *ACS Nano* **2016**, *10*, 3302–3311.
- (44) Svanström, S.; Jacobsson, T. J.; Sloboda, T.; Giangrisostomi, E.; Ovsyannikov, R.; Rensmo, H.; Cappel, U. B. Effect of Halide ratio and Cs⁺ on the photochemical stability of lead halide perovskites. *J. Mater. Chem. A* **2018**, *6*, 22134–22144.
- (45) Green, M. A. *Solar Cells: Operating Principles Technology and System Applications*; The University of New South Wales, 1998.
- (46) Sze, S. M.; Ng, K. K. *Physics of Semiconductor Devices*, 3rd ed.; John Wiley & Sons, Inc., 2007.
- (47) Scheer, R. Activation energy of heterojunction diode currents in the limit of interface recombination. *J. Appl. Phys.* **2009**, *105*, 104505.
- (48) Juarez-Perez, E. J.; Ono, L. K.; Maeda, M.; Jiang, Y.; Hawash, Z.; Qi, Y. Photodecomposition and thermal decomposition in methylammonium halide lead perovskites and inferred design principles to increase photovoltaic device stability. *J. Mater. Chem. A* **2018**, *6*, 9604–9612.
- (49) Tan, W.; Bowring, A. R.; Meng, A. C.; McGehee, M. D.; McIntyre, P. C. Thermal Stability of Mixed Cation Metal Halide Perovskites in Air. *ACS Appl. Mater. Interfaces* **2018**, *10*, 5485–5491.
- (50) Leguy, A. M. A.; Hu, Y.; Campoy-Quiles, M.; Alonso, M. I.; Weber, O. J.; Azarhoosh, P.; van Schilfgaarde, M.; Weller, M. T.; Bein, T.; Nelson, J.; Docampo, P.; Barnes, P. R. F. Reversible Hydration of CH₃NH₃PbI₃ in Films, Single Crystals, and Solar Cells. *Chem. Mater.* **2015**, *27*, 3397–3407.
- (51) Yun, J. S.; Kim, J.; Young, T.; Patterson, R. J.; Kim, D.; Seidel, J.; Lim, S.; Green, M. A.; Huang, S.; Ho-Baillie, A. Humidity-Induced Degradation via Grain Boundaries of HC(NH₂)₂PbI₃ Planar Perovskite Solar Cells. *Adv. Funct. Mater.* **2018**, *28*, 1705363.
- (52) Ning, S.; Zhang, S.; Sun, J.; Li, C.; Zheng, J.; Khalifa, Y. M.; Zhou, S.; Cao, J.; Wu, Y. Ambient Pressure X-ray Photoelectron Spectroscopy Investigation of Thermally Stable Halide Perovskite Solar Cells via Post-Treatment. *ACS Appl. Mater. Interfaces* **2020**, *12*, 43705–43713.
- (53) Chen, S.; Wang, L.-W. Thermodynamic Oxidation and Reduction Potentials of Photocatalytic Semiconductors in Aqueous Solution. *Chem. Mater.* **2012**, *24*, 3659–3666.
- (54) Lei, J.; Gao, F.; Wang, H.; Li, J.; Jiang, J.; Wu, X.; Gao, R.; Yang, Z.; Liu, S. Efficient planar CsPbBr₃ perovskite solar cells by dual-source vacuum evaporation. *Sol. Energy Mater. Sol. Cells* **2018**, *187*, 1–8.
- (55) Lindahl, J.; Zimmermann, U.; Szaniawski, P.; Törndahl, T.; Hultqvist, A.; Salomé, P.; Platzer-Björkman, C.; Edoff, M. Inline Cu(In,Ga)Se₂ Co-evaporation for High-Efficiency Solar Cells and Modules. *IEEE J. Photovoltaics* **2013**, *3*, 1100–1105.
- (56) Sauerbrey, G. Verwendung von Schwingquarzen zur Wägung dünner Schichten und zur Mikrowägung. *Z. Phys.* **1959**, *155*, 206–222.
- (57) Herrera-Gomez, A.; Bravo-Sanchez, M.; Aguirre-Tostado, F. S.; Vazquez-Lepe, M. O. The slope-background for the near-peak regime of photoemission spectra. *J. Electron Spectrosc. Relat. Phenom.* **2013**, *189*, 76–80.
- (58) Shirley, D. A. High-Resolution X-Ray Photoemission Spectrum of the Valence Bands of Gold. *Phys. Rev. B: Solid State* **1972**, *5*, 4709–4714.
- (59) Shofield, H. *Theoretical Photoionization Cross Sections from 1 to 1500 keV*; Lawrence Livermore Laboratory: Livermore, CA, January 1973.